Applied Catalysis B: Environmental 305 (2022) 121019

Contents lists available at ScienceDirect

Applied Catalysis B: Environmental

journal homepage: www.elsevier.com/locate/apcatb

Structural tuning of multishelled hollow microspheres for boosted peroxymonosulfate activation and selectivity: Role of surface superoxide radical

Wenqian Li, Xu He *, Boda Li, Bin Zhang, Ting Liu, Ying Hu, Jun Ma *

State Key Laboratory of Urban Water Resource and Environment, Harbin Institute of Technology, Harbin 150090, China

ARTICLE INFO

Keywords:
Multi-shelled hollow microspheres
Cobalt oxide
Peroxymonosulfate activation
Catalytic selectivity

ABSTRACT

Herein, a multi-shelled hollow micro-reactor with tunable shell number, thickness and porosity is constructed by nanosized Co_3O_4 to catalyze peroxymonosulfate (PMS) for the first time. Triple-shelled hollow microspheres (TS-HM) exhibit superior catalytic activity with the degradation rate of 0.4158 min^{-1}, which is 22, 5.8, 1.9 times of that of solid nanoparticles, quadruple-shelled hollow microspheres (QS-HM), and double-shelled hollow microspheres (DS-HM), respectively. Such an outstanding performance of TS-HM is attributed to more exposed active sites, strong capacity of Co^{II} regeneration and desired structure stability. Furthermore, the selectivity of 2-cholorophenol (2-CP) over humic acid (HA) is optimized by tuning shell thickness and porosity. The thick shell and narrow pore size are recognized as the dominant contributors based on size exclusion effects. Significantly, mechanistic studies reveal that $O_2^{\cdot-}$ is generated on the catalyst surface via O_2 adsorption and reduction by oxygen vacancies, and plays an important role for Co^{II} regeneration.

1. Introduction

Advanced oxidation processes (AOPs) are recognized as highly efficient water treatment technologies via activating a weaker oxidant to create highly reactive radicals for fast degradation of organic pollutants. Distinct from the traditional Fenton system, peroxymonosulfate (PMS) activation has a series of advantages, such as the wider pH adaptability and more reactive oxygen species (ROS) involved in the system (·OH, $SO_4^{\cdot-}$, $O_2^{\cdot-}$, $^1O_2$, etc.) [1,2]. Heterogeneous catalysis is a promising way in response to the limitations of the homogeneous catalysis, such as difficulties in recovery of catalysts and the secondary pollution. With the advantages of large specific surface area (SSA) and quantum confinement effect, various nanomaterials have been used for PMS activation [3,4]. However, considering their ultrafine characteristics, the direct employment of them in practice is challenged, due to the tendency to aggregate, difficulty in handling, and inevitable release to environment [5,6]. Another challenging issue faced in reality is the severely diminished catalytic performance caused by the ubiquitous presence of natural organic matter (NOM), due to blockage of active sites and radical scavenging [7]. Therefore, the design and development of advanced multifunctional catalysts with micron-level dimension, but comparable or even higher catalytic activity than nanomaterials, and specific selectivity for target pollutants are of pivotal importance.

Recently, unique hollow multishelled structures (HoMSs) have attracted considerable attention due to their preeminent properties, including abundant exposed active sites, reduced aggregation of nanosized subunits, efficient mass/electron transfer, confined void space, high loading capacity, and low density [8,9]. In details, the enclosed space of the HoMSs can trap the reactant molecules on active sites and increase the retention time to realize multiple spatial confinement. Meanwhile, the microporous shell with selective permeability can provide size sieving capability to achieve reaction selectivity. Besides, the through-shell mass transport kinetics may affect or even dominate the overall reaction rate, with dependence on the reaction conditions, shell porosity and thickness, as well as the characteristics of reactants which will diffuse through the shell [10]. Therefore, rational tailoring of the shell number, thickness and porosity of HoMSs has significance for enhancement of the catalytic activity and selectivity. Furthermore, from the aspect of practical application, the micron-level HoMSs assembled by nanoparticles are favored owing to their prominent advantages of easy separation and recycling by filtration. In addition, compared with the time-consuming and sophisticated process involving the immobilization of nanocatalysts onto a support, HoMSs can be produced in quantity more easily by facile methods [11–13].

* Corresponding authors.
E-mail addresses: hexu@hit.edu.cn (X. He), majun@hit.edu.cn (J. Ma).

https://doi.org/10.1016/j.apcatb.2021.121019
Received 22 August 2021; Received in revised form 13 December 2021; Accepted 15 December 2021
Available online 21 December 2021
0926-3373/© 2021 Published by Elsevier B.V.

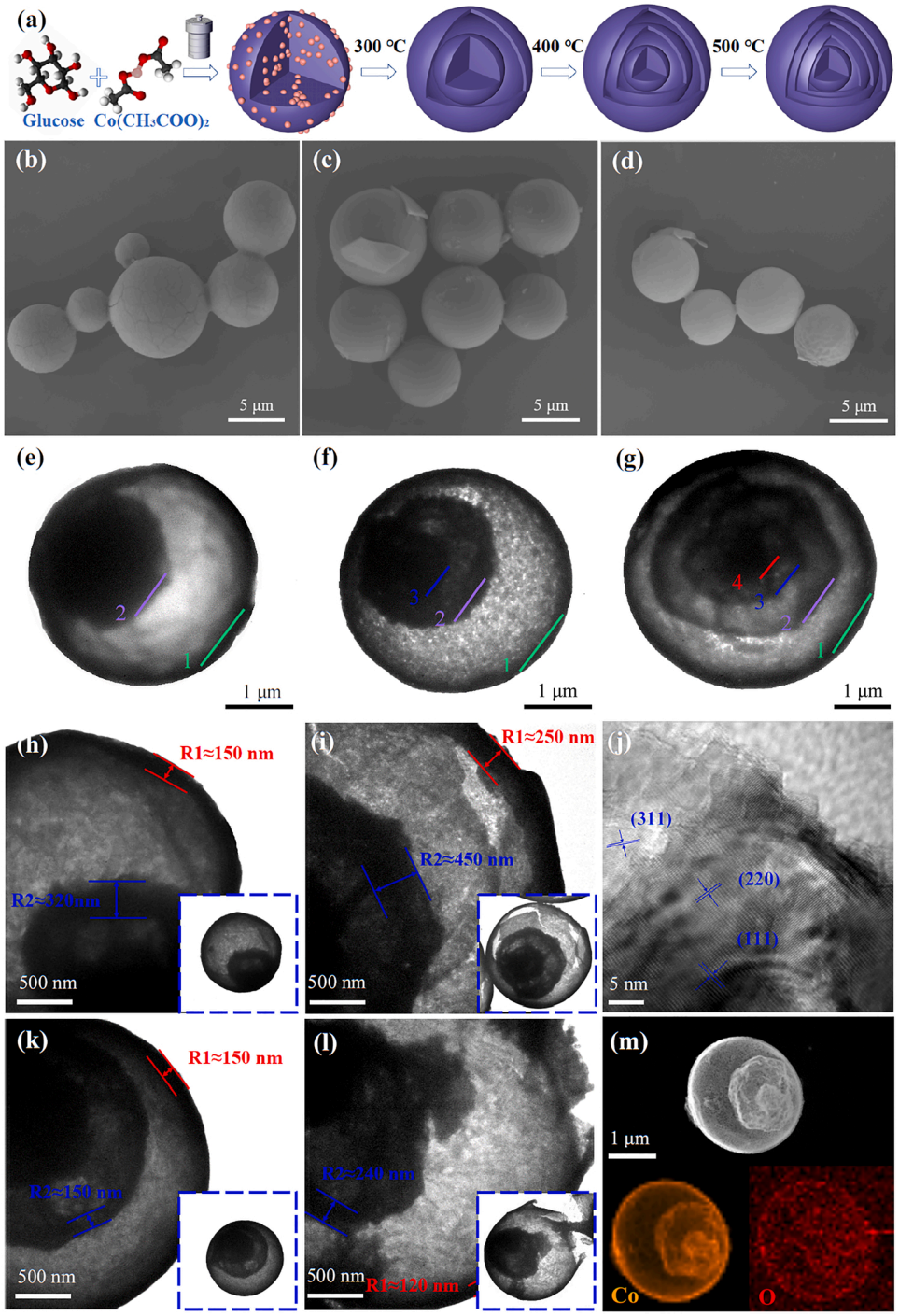

Fig. 1. Synthesis routes for Co_3O_4 MS-HM (a); FESEM images of Co_3O_4 DS-HM-0.7 (b), TS-HM-0.7 (c), QS-HM-0.7 (d); TEM images of DS-HM-0.7 (e), TS-HM-0.7 (f, i), QS-HM-0.7 (g), TS-HM-0.5 (h), TS-HM-1.0 (k), and TS-HM-2.0 (l); HRTEM of the TS-HM-0.7 (j), HAADF-STEM image and EDX element mappings of Co_3O_4 TS-HM-0.7 (m).

Though HoMSs demonstrate aforementioned advantages, so far, only a handful of studies focus on the performance enhancement by the structural regulation of hollow catalysts in the Fenton-like systems. For example, Zhu et al. synthesized cobalt-iron oxides solid, single-, double-, and multi-shelled hollow nanospheres. They conclude that the catalytic activity enhanced with the increasing shell numbers [14]. Zhang et al. find that, compared with the solid and single-shelled hollow nanoparticles, the yolk-shell exhibits superior selectivity in the presence of humic acid (HA) due to the more exposed active sites and effective interception of macromolecules [15]. The enhanced catalytic activity of the yolk−shell nanoreactor was also reported previously in contrast with the solid one [16]. However, to our best knowledge, there is few report concerning multi-shelled hollow microspheres (MS-HM) with tunable shell number, thickness and porosity for simultaneous enhancement of the catalytic activity and selectivity.

To efficiently utilize the active sites and simultaneously enhance the selectivity of target pollutants over HA, herein, Co_3O_4 MS-HM are successfully synthesized by hydrothermal method and the following calcination treatment. The shell number is tuned by calcination temperature, while the shell thickness and porosity are regulated by the molar ratio of

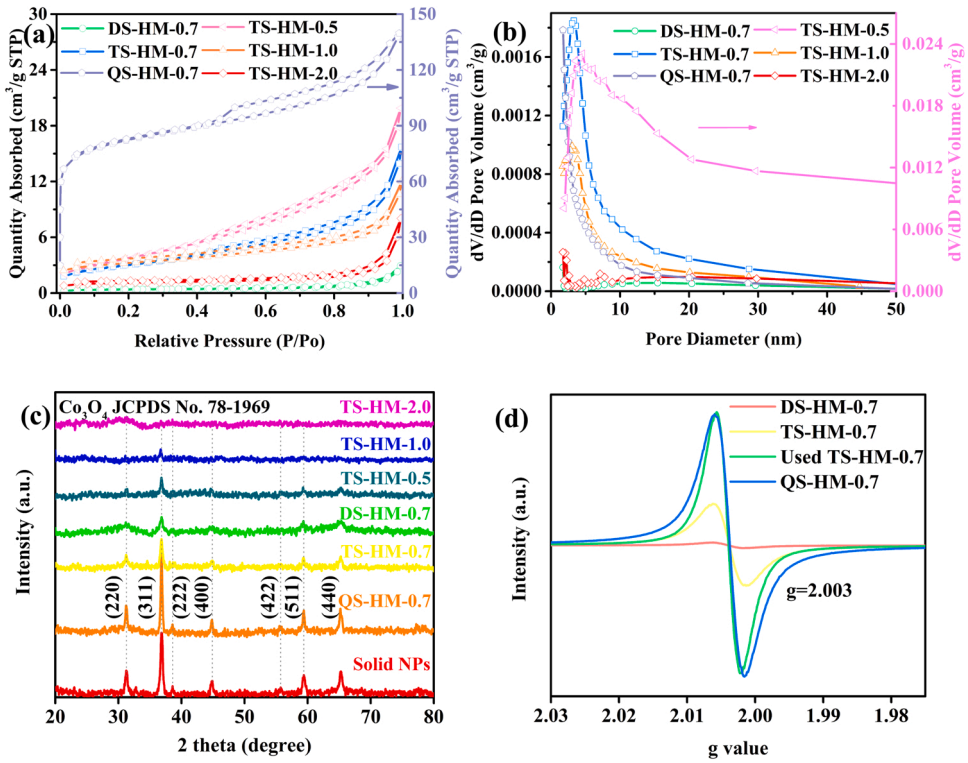

Fig. 2. N_2 adsorption–desorption isotherms (a), pore size distribution curves (b) (The isothermal and distribution data are displayed in a larger scale on the right vertical axis for QS-HM-0.7 and TS-HM-0.5, respectively.), and XRD patterns of Co_3O_4 DS-HM-0.7, TS-HM-0.7, QS-HM-0.7, TS-HM-0.5, TS-HM-1.0, TS-HM-2.0, and solid nanoparticles (c), and solid EPR spectrum of Co_3O_4 DS-HM-0.7, TS-HM-0.7, QS-HM-0.7 and used TS-HM-0.7 after activating PMS (d).

glucose to cobalt acetate. The structure-activity relationship and inherent mechanisms are further explored. Finally, the applicability of the materials is systematically investigated.

2. Experimental section

2.1. Chemicals and characterization method

Detailed information of the chemicals and characterization techniques is available in Text S1 and S2.

2.2. Catalyst preparation

The Co_3O_4 MS-HM were successfully synthesized by a two-step preparation process, namely dewatering at low temperature and carbonization at high temperature [8]. In details, 0.028 mol glucose and 0.040 mol $Co(CH_3COO)_2{\cdot}6H_2O$ were dissolved into 50 mL ultrapure water under magnetic stirring. Subsequently, the obtained solution was transferred into a 100 mL poly(tetrafluoroethylene) (PTFE)-lined stainless-steel autoclave. After hydrothermal treatment at 180 °C for 400 min, the black precipitate of cobalt acetate polysaccharides was centrifuged and rinsed with ultrapure water and anhydrous ethanol for three times. The as-prepared precursors were dried at 60 °C overnight and finally annealed in a muffle furnace at 300, 400, 500 °C for 1 h with a ramping rate of 1 °C/min in air to obtain Co_3O_4 DS-HM-0.7, TS-HM-0.7, QS-HM-0.7, respectively. Co_3O_4 TS-HM with different thickness and pore size can be controlled by tuning the molar ratio of glucose and cobalt acetate (0.5, 0.7, 1.0, 2.0), denoted as TS-HM-X, where X is the glucose/cobalt acetate molar ratio.

2.3. Experimental procedures

The catalytic oxidation experiments were carried out by mixing 100 mL 2-CP solution (50 μM) and 5 mg catalyst in a 150 mL conical flask placed in a water bath at 25 ℃. Magnetic stirring was maintained at 350 rpm during the whole reaction. After the mixture was stirred for one minute to achieve homogeneity, 0.5 mL of 0.1 M PMS stock solution was added to initiate the reaction. These quantities were used in all experiments unless otherwise stated. At given time intervals, 0.5 mL of the liquid samples was withdrawn, filtered through 0.22 μm PTFE membrane filters and mixed with equal volume of methanol to quench the radical reactions. To further study the effect of pH on the degradation process, 0.1 M H_2SO_4 or NaOH was added to adjust the initial pH of the 2-CP solution. For the total organic carbon (TOC) analysis, 1 mL solution sample was collected, filtered, quenched with 1 M Na_2SO_3 solution and diluted 5 times. 2-CP solution was also prepared in tap water (TW), secondary effluent (SE), surface water (SW), underground water (UW) to investigate the effect of different water matrixes. The quenching experiments were performed using specific quenchers including methyl alcohol (MeOH, 500 mM), tert-butanol (TBA, 50 mM), furfuryl alcohol (FFA, 2.5 mM), and p-benzoquinone (pBQ, 25 mM) to discern the generated ROS. To test the reusability and stability, the catalysts were recovered by filtering the samples, washing several times with ethanol and Milli-Q water, and drying at 60 °C in oven. All the degradation experiments were conducted at least duplicates.

2.4. Analytical method

The concentration of pollutant was analyzed by high performance liquid chromatography (Waters 1525, USA) equipped with a Symmetry C18 column (4.6 mm × 150 mm, 5 μm particle size) with a UV detector (Waters 2487, USA) at a wavelength of 280 nm for 2-CP. The mobile phase consisted of methanol and ultrapure water (0.1% (v/v) acetic acid) at the ratio of 60:40 (v/v). The injection volume was 100 μL and the flow rate was 1.0 mL/min with a column temperature of 30 °C. The degradation intermediates of 2-CP were identified using GC-MS/MS (7890B-7000 C, Agilent, USA), equipping with an HP-5 column (30 m × 0.25 mm, ID × 0.32 μm). Total organic carbon (TOC) was determined

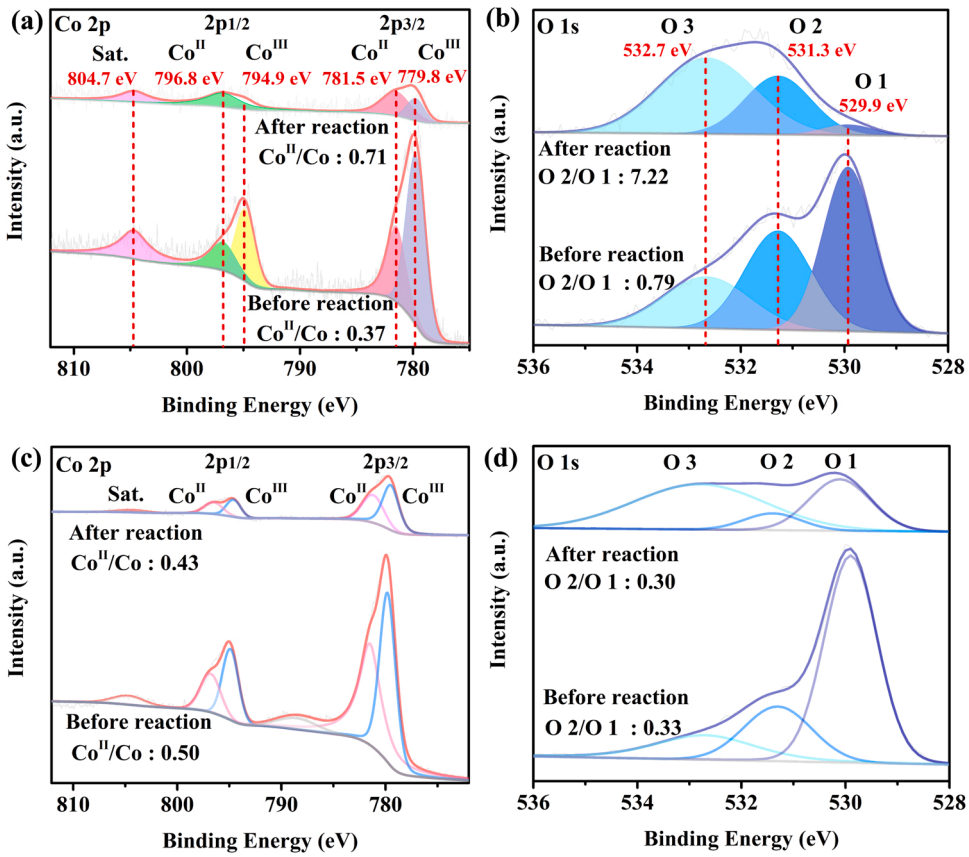

Fig. 3. The high-resolution XPS spectra of Co 2p, and O 1s for as-prepared and PMS treated Co_3O_4 TS-HM-0.7 (a, b) and QS-HM-0.7 (c, d).

with a TOC analyzer (Multi N/C 2100 S, Analytik Jena, Germany). The amount of leaching cobalt was measured by inductively coupled plasma-optical emission spectrometry (ICP-OES) (7300, Perkin Elmer, USA). The concentration of inorganic anions was analyzed by a high performance ion chromatography (Intefrion, ThermoFisher, USA). The concentration of residual PMS was analyzed via iodometric method using a UV–visible spectrophotometer (T6 New century, Puxi General Instruments, Beijing, China). The pH value was adjusted by a pH meter (PHS-3 C, Shanghai Precision & Scientific Instrument, China). The electron paramagnetic resonance (EPR) spectra were monitored using a EPR spectrometer (A300, Bruker, Germany) with 5,5-dimethyl-1-pyrrolidine-N-oxide (DMPO) or tetramethylpiperidine (TEMP) as the spin-trapping agent. The detailed procedure was provided in Text S3.

3. Results and discussion

3.1. Formation and characterization

As illustrated in Fig. 1a, the porous Co_3O_4 MS-HM was synthesized via a one-pot hydrothermal method and subsequent thermal treatment. The cobalt ions were coordinated onto the polysaccharides formed by glucose polymerization to construct a cobalt acetate polysaccharide network as the self-template. MS-HM was then obtained by the oxidization of cobalt ions and the removal of carbon. The shell number, thickness and porosity were controlled by tuning the calcination temperature and the reactant molar ratio, respectively.

Fig. 1b-g show the surface morphology and interior structure of Co_3O_4 DS-HM-0.7, TS-HM-0.7, and QS-HM-0.7. SEM images exhibit perfectly spherical morphology in the micrometer-scale, with the diameters ranging from one to several micrometers (Figs. 1b–d, S1a–c). In addition, TEM images confirm that they possess porous surface and HoMS. Each shell is assembled by nanosized subunits, yielding an inherent porous architecture. It is demonstrated that the shell number can be accurately tuned by the calcination temperature (Fig. 1e–g), while the shell thickness can be roughly tuned by the ratio of glucose to cobalt acetate concentration (Fig. 1h, i, k, and l) [8,17]. Lower cobalt concentration results in smaller nanoparticles, lighter packing and a thinner shell (Table S1). For example, in Figs. 1i and 1l, the shell thickness of TS-HM-0.7 is larger than that of TS-HM-2.0 of identical size. Furthermore, larger nanosized subunits are more tightly packed for TS-HM-0.7. The in-depth crystalline feature of the TS-HM-0.7 is characterized by HRTEM, which exhibits an interplanar spacing of 0.47, 0.29, 0.43 nm corresponding to the crystallographic plane (111), (220), (311), respectively (Fig. 1j). Energy-dispersive X-ray (EDX) element mappings obtained by high-angle annular dark-field scanning transmission electron microscopy (HAADF-STEM) confirms the uniform element distribution (Fig. 1m).

The N_2 adsorption–desorption isotherms with hysteresis loops can be classified as type IV (Fig. 2a), indicating the presence of mesoporous structures. The curve of QS-HM-0.7 exhibits a steep uptake at the relative pressure below 0.01, indicating the existence of micropores in the shells [18]. The hysteresis loops can be classified as type H3, which is associated with slit-shaped pores originated from self-assembly of Co_3O_4 nanosized subunits. They are open at low relative pressure for TS-HM-1.0 and TS-HM-2.0 but closed for the others. The swelling effect could account for the absence of total closure of the hysteresis loops [19]. The SSA, average pore size and pore volume are summarized in Table S1. The SSA of catalysts follow the order of DS-HM-0.7 < TS-HM-2.0 < TS-HM-0.7 ≈ TS-HM-1.0 < TS-HM-0.5 < QS-HM-0.7. Apparently, the SSA becomes larger with the increase in shell number and concentration of metal source. For DS-HM-0.7 and TS-HM-2.0, the pore size distribution is relatively broad, and mainly in the range of 1.7–50.0 nm (Fig. 2b). TS-HM-0.5, TS-HM-0.7, TS-HM-1.0, and QS-HM-0.7 own an average pore diameter centered at around

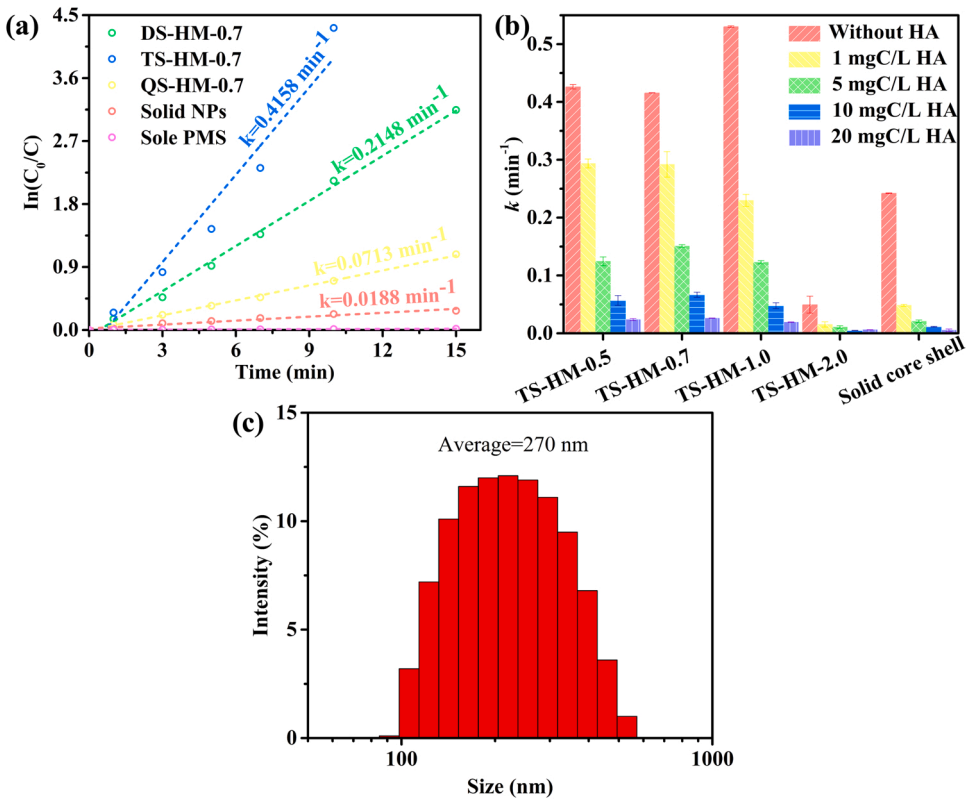

Fig. 4. . 2-CP removal performance of Co_3O_4 solid nanoparticles, DS-HM-0.7, TS-HM-0.7, QS-HM-0.7 (a), TS-HM (0.5, 0.7, 1.0, and 2.0) and solid core-shell sphere with and without HA (b). Reaction conditions: 50 μM 2-CP; 0.5 mM PMS; 0.05 g/L Co_3O_4 TS-HM; 25 °C; Hydrodynamic diameter of HA macromolecules measured by a zetasizer (c).

4.56 nm, 3.30 nm, 3.05 nm, and 1.73 nm, respectively.

The XRD peaks in Fig. 2c can be indexed as the cubic spinel Co_3O_4 crystalline structure which has the Fd3^{-}m (227) space group (JCPDS Card No. 78–1969). No characteristic diffraction peaks ascribed to CoO, Co_2O_3 or metallic Co are found, indicating the successful fabrication of Co_3O_4 of high phase purity. The peak intensity narrows and sharpens as calcination temperature increases from 300 ℃ to 500 ℃, while it greatly broadens and weakens as the glucose-to-cobalt molar ratio increases from 0.5 to 2.0. Both the crystallinity degree and crystalline size of cubic Co_3O_4 increase with increasing calcination temperature and cobalt content (Table S1), indicating that Co_3O_4 MS-HMs recrystallize and grow at higher temperature. Additionally, the intensity of the peak at g= 2.003 increases with increasing calcination temperature (300 ℃–500 ℃), which is indicative of the elevating content of oxygen vacancy (Fig. 2d).

XPS analysis was carried out to determine the surface chemical composition and element valence state of TS-HM. The survey XPS spectra display characteristic peaks of C 1s, O 1s, Co 2s, Co 2p, Co 3s and Co 3p, confirming the presence of cobalt and oxygen elements in the Co_3O_4 TS-HM (Fig. S2). In addition to one shake-up satellite peak at 804.7 eV, the high-resolution Co 2p spectra exhibit two main peaks at approximately 794.9 eV (796.8 eV for the used Co_3O_4 TS-HM) and 779.9 eV associated with the doublet Co $2p_{3/2}$ and Co $2p_{1/2}$ regions, respectively (Fig. 3a) [20]. After deconvolution, the Co $2p_{3/2}$ displays two peaks at 779.8 and 781.5 eV, corresponding to Co^{III} and Co^{II}, respectively [21,22]. The binding energies at 794.9 and 796.8 eV are attributed to Co $2p_{1/2}$ peaks of Co^{III} and Co^{II} ions, respectively [23]. The surface relative Co^{II} /Co^{III} atomic ratio is calculated to be ~0.5 for as-prepared Co_3O_4 TS-HM (Table S2), in consistent with the stoichiometric ratio for Co_3O_4, which contains two types of cobalt ions, Co^{II} in tetrahedral sites and Co^{III} in octahedral sites in the ratio of 1:2. The O 1s spectra can be decomposed into three components: peak I ascribed to lattice oxygen in metal oxide at lower binding energy from 529.4 to 530.0 eV, peak II assigned to the presence of non-stoichiometric oxygen in the surface region at binding energy between 530.5 and 532.0 eV, and peak III associated with weakly surface-bounded oxygen of the contamination species in the range of 532.7–533.3 eV [20]. In Fig. 3b, the peaks at 529.9 eV, 531.3 eV, and 532.7 eV are ascribed to lattice oxygen (O 1), defective oxygen (O 2), and surface absorbed moisture or contamination species (O 3), respectively [24,25]. The XPS analysis is also conducted for the used TS-HM-0.7, and the comparative analysis of TS-HM-0.7 before and after catalytic reaction will be discussed in the Section 3.3.

3.2. Catalytic performance

2-CP adsorption within 15 min is almost negligible (only 0.3%, 2.0%, 0.4% for Co_3O_4 DS-HM-0.7, TS-HM-0.7, QS-HM-0.7 respectively) by the catalysts alone, indicating the weak contribution of adsorption. Meanwhile, in the absence of catalysts, percentage of 2-CP degradation is merely 1.8% by sole PMS. However, 95.7%, 100%, 66.1% of 2-CP was catalytically oxidized by DS-HM-0.7/PMS, TS-HM-0.7/PMS, and QS-HM-0.7/PMS system, respectively. This implies that 2-CP is mainly degraded via PMS activation. The reaction rate constant of Co_3O_4 DS-HM-0.7, TS-HM-0.7, QS-HM-0.7 is 11, 22 and 3.8 times higher than that of the rigid Co_3O_4 nanospheres, respectively (Fig. 4a). 60.4% of the chlorine atom was released from the aromatic ring after 1 h for Co_3O_4 TS-HM-0.7. The comparison of catalytic activity and durability with previous reported metal oxide/sulfide catalysts are listed in Table S3. The superior catalytic activity of HoMS can be attributed to the existence of confinement effect induced by inner voids [5,15,16,26]. Benefit from high SSA and porosity, Co_3O_4 TS-HM-0.7 displays better degradation performance than DS-HM-0.7. Surprisingly, Co_3O_4 QS-HM-0.7 with the highest SSA, shell number, and oxygen vacancies shows the slowest

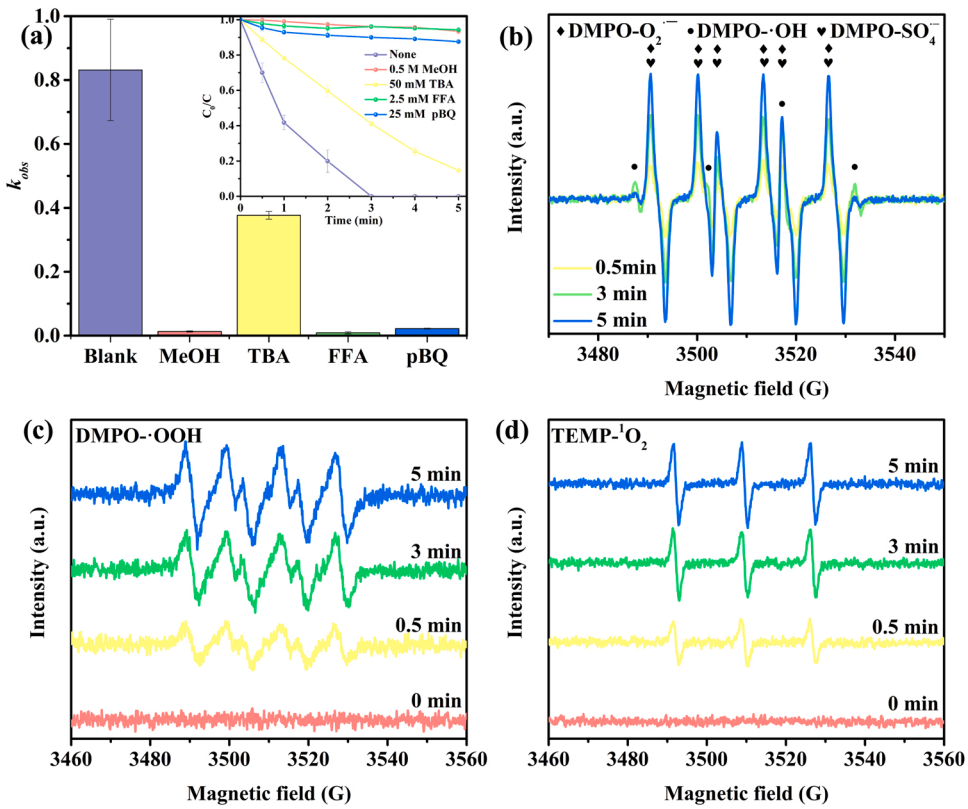

Fig. 5. Influences of different quenchers on the Co_3O_4 TS-HM-0.7/PMS system for 2-CP degradation. Error bars represent one standard deviation for two repeated experiments (a); DMPO-trapped EPR spectra for the detection of ·OH and $SO_4^{\cdot-}$ using water as the solvent over time (DMPO-·OH with hyperfine splitting constants $a_N = a_H = 14.95$ G; DMPO-$SO_4^{\cdot-}$ with hyperfine splitting constants $a_N = 13.2$ G, $a_H = 9.60$ G, $a_H = 1.48$ G and $a_H = 0.78$ G) (b); DMPO-trapped EPR spectra for the detection of $O_2^{\cdot-}$ using methanol as the solvent over time (DMPO- $O_2^{\cdot-}$ with hyperfine splitting constants $a_N = 13.2$ G, $a_H = 9.60$ G, $a_H = 1.48$ G and $a_H = 0.78$ G) (c); and TEMP-trapped EPR spectra for the detection of $^1O_2$ using water as the solvent over time (d).

degradation compared with DS-HM-0.7 and TS-HM-0.7. It can be explained by the capacity of Co^{II} regeneration and structure stability (Fig. 3) [8]. Specifically, in the TS-HM-0.7/PMS system, Co^{II} increases along with the loss of lattice oxygen, but an opposite phenomenon is observed in QS-HM-0.7/PMS system. This phenomenon indicates that the TS-HM-0.7 owns a higher degree of Co_{oh}^{III}-O covalency and lower charge transfer energy to favor the interaction between Co_{oh}^{III} and O species (lattice oxygen/*OSO_3OH /*OH), compared with QS-HM-0.7 [27].

The influence of glucose/cobalt acetate ratio on 2-CP degradation is further explored. In Fig. 4b, the reaction rate drops drastically from 0.53 min^{-1} to 0.06 min^{-1} as the glucose/cobalt acetate ratio increases from 1.0 to 2.0. This result can be explained by the fact that the HoMS is not maintained well for TS-HM-2.0. Furthermore, the reaction rate of TS-HM-1.0 with lower shell thickness of 150 nm is higher than that of TS-HM-0.5 and TS-HM-0.7, indicating the less restricted transport through the shell of TS-HM-1.0. The results are consistent with previous studies which indicate that very narrow micropores and thick shell may limit the substantial diffusion under the specific reaction conditions [28].

The catalytic performance of TS-HM with different shell thicknesses and pore sizes is further evaluated in the system containing multiple pollutants. HA, the macro-molecule widespread in natural waters, is selected to explore the selectivity of TS-HM/PMS system for the target pollutant 2-CP. In the existence of 1 mgC/L HA, the reaction rate drops by 31%, 29%, 57% and 80% for Co_3O_4 TS-HM-0.5, TS-HM-0.7, TS-HM-1.0, and solid core shell sphere respectively. This phenomenon confirms the existence of the size sieving capacity of HoMSs (Fig. 4b, Fig. S3). TS-HM-0.7 with quite thick shell and relatively narrow pore size show the lowest decline of reaction rate, demonstrating the selectivity of 2-CP over HA distinctly. This special catalytic selectivity can be explained by the molecular sieving effect: 2-CP has a small molecular size of 5.76 × 4.82 Å, while HA macromolecule has a hydrodynamic diameter of ~270 nm (Fig. 4c) [29,30]. The confined voids of the TS-HM are only accessible to the small reactants with molecular size below the pore size of the shell. The reactants will be enriched in the voids, accounting for increased reaction rates. Therefore, the porous shells with certain thickness and pore size act as catalytic filters and displays molecular sieving properties. The through-shell diffusion kinetics are highly dependent on these structural parameters, since the diffusion limitations may be induced by the shell with narrow micropores and large thickness. Large thickness denotes the long diffusion distance, contributing to the diffusion limitations and size sieving effect. Optimization of these structural parameters will enhance the separation efficiency and catalytic selectivity, by means of controlling the molecular traffic to more active sites. In addition, after being catalytically oxidized by the outermost shell, HA itself becomes more hydrophobic and re-aggregated into larger flocs with higher hydrodynamic diameter, further enhancing the molecular sieving effect and catalytic selectivity of the hydrophilic TS-HM [30].

3.3. Degradation mechanism and pathway

To preliminarily ascertain the type and contribution of ROS involved in the TS-HM-0.7/PMS system, a series of quenching experiments were conducted with different radical scavengers. In Fig. 5a, complete removal was achieved in 3 min without any quenchers, while only 3.9% of 2-CP was degraded with addition of MeOH, a commonly used quencher for ·OH and $SO_4^{\cdot-}$, and in the presence of TBA, the degradation efficiency is decreased to 58.9%. It indicates that ·OH and $SO_4^{\cdot-}$ are the dominant ROS responsible for the 2-CP degradation. Nevertheless, the contribution of $O_2^{\cdot-}$ and $^1O_2$ to 2-CP is negligible. Surprisingly, in the presence of pBQ, as the exclusive scavenger for $O_2^{\cdot-}$ (k_{BQ}=2.9 ×10^9 M^{-1} S^{-1}) [31], the degradation rate also declines markedly. In addition, the presence of $O_2^{\cdot-}$ was further confirmed with nitrotetrazolium blue chloride (NBT) as the chemical probe (Fig. S4). Based on these results, we deduce that although $O_2^{\cdot-}$ does not degrade 2-CP directly, it still plays an important role for the generation of ·OH and $SO_4^{\cdot-}$, and

participates in the 2-CP degradation indirectly in the TS-HM-0.7/PMS system. It should also be noted that FFA, as the scavenger of $^1O_2$, also inhibits the 2-CP degradation substantially. However, the result is misleading because FFA can also scavenge ·OH and $SO_4^{\cdot-}$ at a relatively high rate constant, leading to the overestimation of the role of $^1O_2$. Besides, by kinetic calculation (details are provided in Text S4), the reaction rate of $^1O_2$ with water is 548-fold more than that with 2-CP, indicating the contribution of $^1O_2$ to 2-CP oxidation is negligible.

EPR technique was employed to further confirm the ROS produced during the PMS activation. Distinct from previous studies [32,33], there are no prominent four-line spectrum of DMPO-·OH (1:2:2:1) or six-line spectrum of DMPO-$SO_4^{\cdot-}$ (1:1:1:1:1:1), while the sextet peaks of DMPO-$O_2^{\cdot-}$ adduct are exhibited clearly in the aqueous solution (Fig. 5b). By further spectral simulation, the characteristic signals of DMPO-$O_2^{\cdot-}$, DMPO-$SO_4^{\cdot-}$, and DMPO-·OH adducts can be identified simultaneously (Fig. S5) [15]. Besides, the characteristic signals of DMPO-$O_2^{\cdot-}$ are also observed in MeOH, demonstrating the existence of $O_2^{\cdot-}$ (Fig. 5c). Considering the fact that, in most cases, the distinct sextet peaks of DMPO-$O_2^{\cdot-}$ adduct are only observed in the presence of MeOH, due to low stability of $O_2^{\cdot-}$ in water, long lifetime in MeOH, and no interference from DMPO-·OH and DMPO-$SO_4^{\cdot-}$. It can be inferred that $O_2^{\cdot-}$ should exist on the catalyst surface with high reactivity and be generated from reduction of dissolved molecular oxygen by electrons trapped in oxygen vacancies [34]. To further prove this conjecture, the experiment was also performed under anaerobic conditions by Ar bubbling for 1 h ahead of reaction. The Ar gas bubbling exerts distinct influence on 2-CP degradation, with reaction rate decreasing evidently from 0.512 min^{-1} under the aerobic condition to 0.063 min^{-1} in the experiment the deoxygenated experiment was performed under anaerobic conditions by Ar bubbling for 1 h ahead of reaction (Fig. S6). The result demonstrates that $O_2^{\cdot-}$ is originated from O_2 reduction by localized electrons in oxygen vacancies. In addition, a three-line spectrum of TEMP-$^1O_2$ (1:1:1) is found to increase with the reaction time (Fig. 5d). Generally, $^1O_2$ can be originated from the recombination or disproportion of $O_2^{\cdot-}$, the reaction between $SO_5^{\cdot-}$ and H_2O, and self-decomposition of PMS.

In summary, there are four kinds of ROS detected in the Co_3O_4 TS-HM-0.7/PMS system, namely, ·OH, $SO_4^{\cdot-}$, $O_2^{\cdot-}$ and $^1O_2$. Thereinto, ·OH and $SO_4^{\cdot-}$ contribute dominantly to the 2-CP degradation. $O_2^{\cdot-}$ indirectly participates in the 2-CP degradation, and $^1O_2$ plays an insignificant role.

To figure out the active sites for PMS activation, XPS was utilized to compare the variation in the chemical states of the as-prepared and used Co_3O_4 TS-HM-0.7. As shown in Fig. 3a, after the PMS activation process, the proportion of Co^{II} increases markedly from 37% to 71%, indicating Co^{III} is reduced to Co^{II} during PMS activation. There are two aspects of the reasons that may account for the increased Co^{II}/ Co^{III} molar ratio. On the one hand, Co^{II} could be regenerated from Co^{III} at the expense of PMS consumption, based on the common knowledge that Co^{II} activates PMS to produce $SO_4^{\cdot-}$ and Co^{III}, and then Co^{III} can be reduced back to Co^{II} (Eqs. 1–3). On the other hand, $O_2^{\cdot-}$ on the catalyst surface transfers electron to Co^{III} via oxygen vacancies, thus accelerating the transformation of Co^{III} to Co^{II} (Eqs. 5–6). The standard redox potential of Co^{III}/Co^{II} and $O_2^{\cdot-}/O_2$ is 1.81 V and − 0.33 V, respectively [2,35]. Consequently, the reduction of Co^{III} by $O_2^{\cdot-}$ is thermodynamically feasible. The importance of $O_2^{\cdot-}$ is also proved in the quenching experiment where the degradation rate is inhibited remarkedly in the presence of pBQ. Besides, it is reported that 2-CP or its intermediate hydroquinone can also serve as electron donators to achieve a redox cycling of Co^{III} and Co^{II} [34,35]. However, in our study, the activation of PMS is not accelerated by the addition of 2-CP but inhibited slightly (Fig. S7), suggesting that pollutants are not electron donators.

Apart from Co species, O species also experienced obvious changes. The ratio of O 2 to O 1 (a yardstick to estimate the relative amount of surface oxygen vacancies) rises from 0.79 to 7.22 (Fig. 3b), indicating that O 1 is consumed substantially, along with the rise in O 2. The existence of O 2 was also confirmed by the solid EPR with a peak at g = 2.003 (Fig. 2d). The signal intensity of the spent catalyst is enhanced, compared with that of the fresh catalyst, verifying the O 2 content increased after catalytic reaction. Actually, the increase in Co^{II} will lead to the release of O 1 to maintain the surface charge balance and the production of O 2 [24,36]. Meanwhile, the consumption of O 1 could also be caused by the reduction of $SO_5^{\cdot-}$ to $SO_4^{\cdot-}$ (Eq. 7). The increase in O 2 exactly accounts for the increasing intensity of DMPO- $O_2^{\cdot-}$ (Figs. 5b and 5c). For O 3, the increased proportion of it after reaction is due to the contamination of catalyst surface by oxygen species originated from 2-CP transformation and water molecules.

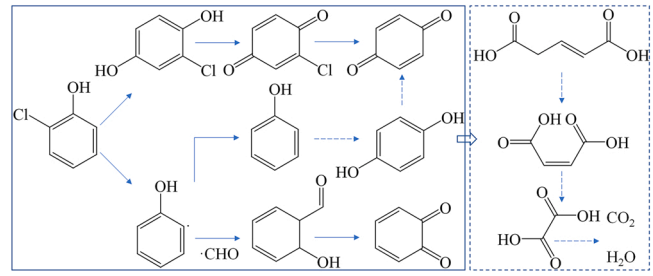

Fig. 6. Possible degradation pathways of 2-CP.

$$\equiv CoOH^+ + HSO_5^- \rightarrow \equiv CoO^+ + SO_4^{\cdot-} + H_2O \quad (1)$$

$$\equiv CoO^+ + 2H^+ \rightarrow \equiv Co^{3+} + H_2O \quad (2)$$

$$\equiv Co^{3+} + HSO_5^- \rightarrow \equiv Co^{2+} + SO_5^{\cdot-} + H^+ \quad (3)$$

$$SO_4^{\cdot-} + H_2O \rightarrow HSO_4^- + {}^{\cdot}OH \quad (4)$$

$$O_2 + V_o + e^- \rightarrow O_2^{\cdot-} \quad (5)$$

$$\equiv Co^{3+} + O_2^{\cdot-} \rightarrow \equiv Co^{2+} + O_2 \quad (6)$$

$$SO_5^{\cdot-} + O^{2-} \rightarrow SO_4^{\cdot-} + O_2 + V_o \quad (7)$$

Based on the above analysis of ROS and catalyst, the degradation mechanism for Co_3O_4 TS-HM-0.7/ PMS is tentatively proposed as follows. PMS activation is initiated via its adsorption on the positively charged catalyst surface and the electron transfer from catalysts to PMS. Oxygen vacancies, usually found on the surface of transition metal oxide, capture and reduce the ambient O_2 by trapped electrons to generate $O_2^{\cdot-}$ on the solid surface which demonstrated much stronger reactivity than those in the aqueous solution [34]. A fast reduction of Co^{III} to Co^{II} is achieved by PMS and $O_2^{\cdot-}$, and high proportion of Co^{II} will further contribute to the release of bulk lattice oxygen and the production of oxygen vacancies. In general, lattice oxygen is sacrificed to maintain the Co^{II}/ Co^{III} cycle and achieve fast PMS activation.

The GC–MS/MS analysis reveals the presence of phenol, 2-chlorohydroquinone (CHQ), BQ and 2-hydroxy benzaldehyde (HB) (Fig. S8). The possible degradation pathway is proposed in Fig. 6. In details, 2-CP molecules are firstly dechlorinated to form phenol or changed to CHQ through ·OH addition. HB is produced by the combination of phenol and formyl radical. CHQ could be further dechlorinated and oxidized to form p-BQ, while HB would be oxidized to o-BQ. Based on previous studies, BQ was oxidized stepwise to low toxic glutaconic acid, maleic acid, oxalic acid, formic acid via benzene ring cleavage, and finally mineralized to CO_2 and H_2O [37].

3.4. Effect of reaction parameters

Solution pH usually influences the PMS activation and 2-CP removal to a great extent, as it affects the existence forms of PMS, 2-CP and the surface charge of catalysts. The pseudo-second-order kinetic plot in the range of 3–11 is presented in Fig. 7a. The k_{obs} in the range of 4–10 is larger than that at very acidic or alkaline conditions (pH 3 or pH 11). It

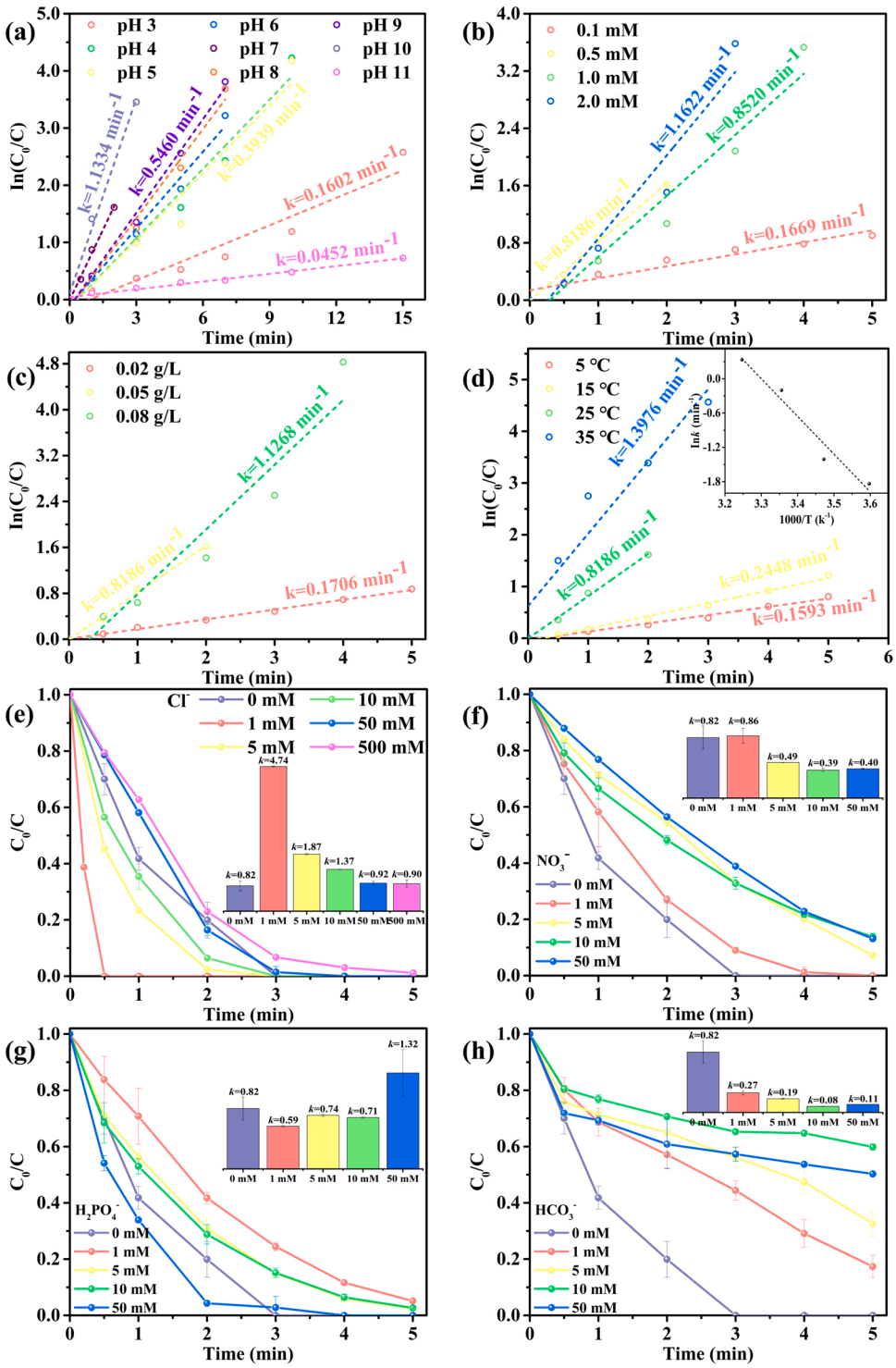

Fig. 7. Effects of initial pH (Initial pH denotes the solution pH before PMS addition) (a), PMS concentration (b), catalyst dosage (c), and temperature (d), Cl^- ions (e), NO_3^- ions (f), $H_2PO_4^-$ ions (g), and HCO_3^- (h) on 2-CP degradation. Reaction conditions: 50 μM 2-CP; 0.5 mM PMS; 0.05 g/L Co_3O_4 TS-HM-0.7; Initial pH 7.0; 25 °C. Error bars represent one standard deviation for two repeated experiments.

can be explained by several aspects. The surface of Co_3O_4 TS-HM-0.7 is positively charged due to its isoelectric point (IEP) around 10.4 (Fig. S9). Therefore, even at basic pH, hydroxyl groups at the surface of Co_3O_4 TS-HM-0.7 can be regenerated readily from the interaction of cobalt species with H_2O, which is the rate limiting step for PMS activation. Besides, positively charged surface results in a high affinity between PMS and the catalysts, facilitating the PMS activation. Instead, the catalytic activity will reduce at pH> IEP. The stability of PMS is also pH dependent. At very low pH, H_2SO_5, the protonated forms of PMS, becomes the main species. At pH> 9.40 (pKa of PMS), SO_5^{2-}, as the deprotonated forms of PMS, becomes the main species. Furthermore, the neutral forms of phenols have less reactivity to $SO_4^{\cdot-}$ and ·OH than phenolate forms [38]. The reactivity of 2-CP increases with the increasing deprotonation degree. However, this is not the case for PMS. Consequently, the suitable pH depends on the combined effects of 2-CP and PMS speciation.

Fig. 7b exhibits the effect of PMS amount on the degradation rate of

2-CP. From 0.1–0.5 mM, the k_{obs} increases markedly from 0.17 to 0.82 min^{-1}. However, when further increasing the PMS, the increase in k_{obs} is not very evident. This can be attributed to the limited catalyst loading or PMS self-quenching. TOC removal is 36.3%, 41.4%, 43.7%, 45.6% for the case of 0.1, 0.5, 1.0 and 2.0 mM, respectively (Fig. S10a). 84.2% of PMS was decomposed by 0.05 g/L catalysts at the PMS dosage of 0.1 mM (Fig. S10b). The PMS utilization efficiency (△(2-CP)/△PMS) is 0.57,0.96,0.53, 0.30 for the case of 0.1, 0.5, 1.0 and 2.0 mM, respectively. 0.5 mM is the most suitable dosage of PMS for activating Co_3O_4 TS-HM-0.7 (0.05 g/L) to treat 2-CP (50 μM). The utilization efficiency decreased when the initial dosage was above 0.5 mM, denoting the occurrence of PMS self-quenching. As showed in Fig. 7c, the degradation rate increased with the catalyst loading. The k_{obs} increased from 0.17 to 1.13 min^{-1} by increasing catalyst loading of 0.02–0.08 g/L. This indicates that the reaction rate is determined greatly by the content of catalytic active sites. Elevation in temperature can also accelerate the reaction (Fig. 7d).

3.5. Effect of common water matrixes and anions

To explore the practical application of the Co_3O_4 TS-HM-0.7/PMS system, different real water samples, including tap water (TW), river water (RW), underground water (UW), and secondary effluent (SE), were used as the water matrices to evaluate the catalytic activity of the Co_3O_4 TS-HM-0.7. The water quality parameters are listed in Table S4. In 5 min, the degradation efficiency is 100%, 68.9%, 64.6%, and 57.6% in the TW, RW, UW, and SE, respectively (Fig. S11). Interestingly, the degradation rate in the TW is higher than that in the UW. This is probably due to relatively high concentration of Cl^-.

Anions are pervasive in natural waters and influence the radical based reactions to various extent. Anions are pervasive in natural waters and influence the radical based reactions to various extent. Fig. 7e–h shows the kinetic curves of 2-CP degradation carried out in ultrapure water and in the presence of different anions with varied strengths. Only Cl^- exhibits promotion effect on 2-CP degradation in the range of 0–500 mM. Complete removal can be achieved only in 30 s, 3 min, 4 min, 6 min in the presence of 1 mM, 10 mM, 50 mM, and 500 mM Cl^-, respectively. With 1 mM Cl^- added, the degradation rate reaches the highest. The promotion effect of Cl^- in PMS based oxidation system was also reported by in previous studies [39]. $SO_4^{\cdot-}$, $SO_5^{\cdot-}$ and ·OH can react with Cl^- to produce less reactive chlorine species, including Cl_2, HOCl, $Cl_2^{\cdot-}$ and $Cl^{\cdot}$ (Eqs. 8–13). However, the reactive chlorine species might participate in the 2-CP degradation more selectively to offset the rate losses caused by radical scavenging [40]. Although chlorine radicals are involved in the system, they have an insignificant impact on the mineralization degree at neutral pH (Fig. S12).

Degree of inhibition is mainly associated with the reaction rate between anions and radicals, activity of resulting radicals, and degree of complexation between metal site and anions (Eqs. 14–19). The inhibition effect is diminished follows the order of $HCO_3^- > NO_3^- > H_2PO_4^-$, just in accordance with the order of their reaction rate with radical. It denotes the inhibition is highly dependent on the reactivity of radical with anions. HCO_3^- would result in a rise in pH, as an alkalinity anion. Nevertheless, the inhibition effect of HCO_3^- is much stronger. This is because HCO_3^- serves as an efficient scavenger to react with $SO_4^{\cdot-}$, ·OH and $O_2^{\cdot-}$, producing less active radicals. Apart from radical scavenging, HCO_3^- could consume PMS to form HCO_4^-. Besides, pH dropped to 3–5 after PMS addition, the resulting CO_2 is not conducive to the generation $O_2^{\cdot-}$. $H_2PO_4^-$ shows the dual effects. At low dosage from 1 to 10 mM, it shows the inhibition effect due to its competition with PMS for active sites and with 2-CP for radicals. Nevertheless, the promotion effect is observed at 50 mM, possibly because additional phosphate can directly activate PMS to produce sulfate radicals and promote pollutant degradation [41,42]. For NO_3^-, a drop in k_{obs} can be observed with concentration increasing from 1 mM to 5 mM. Above 5 mM, change in NO_3^- dosage has a subtle effect on the k_{obs}.

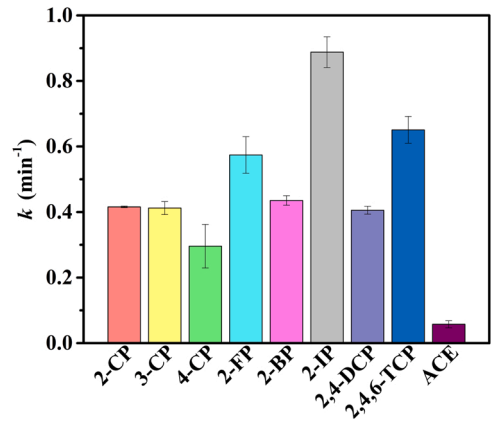

Fig. 8. Degradation efficiencies of other phenolic compounds in the Co_3O_4 TS-HM-0.7/PMS system. Reaction conditions: 50 μM pollutant; 0.5 mM PMS; 0.05 g/L Co_3O_4 TS-HM-0.7; Unadjusted pH; 25 °C. Error bars represent one standard deviation for two repeated experiments.

$$SO_4^{\cdot-} + Cl^- \rightarrow SO_4^{2-} + Cl^{\cdot}\ k = 2{\cdot}1 \times 10^8\ M^{-1}s^{-1} \quad (8)$$

$$^{\cdot}OH + Cl^- \rightarrow OH^- + Cl^{\cdot}\ k = 4{\cdot}2 \times 10^9\ M^{-1}s^{-1} \quad (9)$$

$$Cl^{\cdot} + Cl^- \rightarrow Cl_2^{\cdot-}\ k = 8{\cdot}5 \times 10^9\ M^{-1}s^{-1} \quad (10)$$

$$Cl_2^{\cdot-} + Cl_2^{\cdot-} \rightarrow Cl_2 + 2Cl^- \quad (11)$$

$$Cl^{\cdot} + Cl^{\cdot} \rightarrow Cl_2 \quad (12)$$

$$Cl_2 + H_2O \rightarrow HClO + H^+ + Cl^- \quad (13)$$

$$SO_4^{\cdot-} + HCO_3^- \rightarrow SO_4^{2-} + CO_3^{\cdot}\ k = 1{\cdot}6 \times 10^6\ M^{-1}s^{-1} \quad (14)$$

$$^{\cdot}OH + HCO_3^- \rightarrow H_2O + CO_3^{\cdot-}\ k = 8{\cdot}5 \times 10^6\ M^{-1}s^{-1} \quad (15)$$

$$SO_4^{\cdot-} + NO_3^- \rightarrow SO_4^{2-} + NO_3^{\bullet}\ k = 5{\cdot}5 \times 10^5\ M^{-1}s^{-1} \quad (16)$$

$$^{\cdot}OH + NO_3^- \rightarrow OH^- + NO_3^{\bullet}\ k < 5{\cdot}0 \times 10^5\ M^{-1}s^{-1} \quad (17)$$

$$SO_4^{\cdot-} + H_2PO_4^- \rightarrow SO_4^{2-} + H_2PO_4^{\bullet}\ k < 7{\cdot}2 \times 10^4\ M^{-1}s^{-1} \quad (18)$$

$$^{\cdot}OH + H_2PO_4^- \rightarrow OH^- + H_2PO_4^{\bullet}\ k = 2{\cdot}0 \times 10^4\ M^{-1}s^{-1} \quad (19)$$

3.6. Universality and reusability

The degradation rate of the monochlorophenols (MCPs) follows the order of 2-CP > 3-CP > 4-CP (Fig. 8). It demonstrates that the chlorine position of MCP affects the reactivity. But for Fenton's agent, the degradation rate of 3-CP is usually faster than 2-CP and 4-CP, due to directory effect (OH and Cl groups are *ortho* and *para* directors) [43]. This reflects different reaction mechanisms dominated in $SO_4^{\cdot-}$ and ·OH based systems.·OH is prone to attack organics by hydroxyl addition or hydrogen abstraction while $SO_4^{\cdot-}$ reacts more selectively via electron transfer (electrophilic attack). The reactivity of MCPs mainly depends on an overall result of the electron withdrawing inductive effect, π-electron donating conjugative effect, steric hindrance effect, and directory effect [43]. In the Co_3O_4 TS-HM-0.7/PMS system, the steric hindrance effect and electron withdrawing inductive effect from 2-CP could be neglected. 4-CP is more difficult to degrade than 3-CP, since π-electron donating conjugative effect of chlorine at *meta* positions is more significant. It is generally accepted that with chlorine content increasing, the negative effects will be magnified including hydrophobicity, electron withdrawing inductive effect, steric hindrance effect, and directory effect. However, from the order of the degradation rate: 2,4,6-TCP > 2-CP > 2,4-DCP > 4-CP, it can be concluded that the substitution of chlorine at

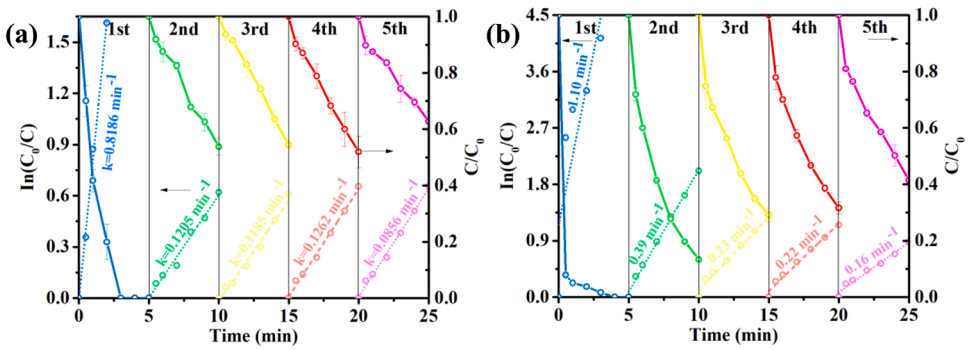

Fig. 9. The recycling performance of Co_3O_4 TS-HM-0.7 for 2-CP degradation at pH 3.7 (a), and 7.0 (b). Reaction conditions: 50 μM 2-CP; 0.5 mM PMS; 0.05 g/L Co_3O_4 TS-HM-0.7; 25 °C. Error bars represent one standard deviation for three repeated experiment.

ortho position on the aromatic ring does accelerate the degradation rate and the substitution position has a more significant effect on the reactivity than the substitution number. The degradation rate of halogenated phenols follows the order of 2-IP > 2-FP > 2-BP > 2-CP. According to the electronegativity of the halogens, the electron withdrawing inductive effect and acidity decrease in the order of 2-FP > 2-CP > 2-BP > 2-IP. The donating conjugative effect decreases in the same order due to the degree of orbit overlap. The difference in degradation rate might result from a balance of inductive effect and conjugative effect.

The acetamino group belongs to activating groups, which increase the electrophilic reactivity. Thus, ACE is usually considered to have a higher degradation rate than that of 4-CP in the electrophilic reactions. However, in our system, it exhibits the slowest degradation rate. This could be explained by the bigger molecular size of ACE (1.19 nm × 0.75 nm × 0.46 nm) [29,44]. The mass transfer is relatively poor as a bigger molecule diffuses through the shell of certain thickness and into confined voids. In conclusion, the Co_3O_4 TS-HM-0.7/PMS system could be an efficient method for removal of halogenated phenols.

The stability and reusability of catalysts are evaluated by successive batches of catalytic degradation under identical reaction condition. At pH of 3.7 (initial pH=7.0), the degradation efficiency decreased after the first cycle but remains unchanged afterwards (Fig. 9a). Noteworthy, when pH of the 2-CP solution was adjusted to 7.0 as the initial state, it will decrease to ~3.7 immediately after the addition of 0.5 mM PMS and continue to decrease slightly during catalytic oxidation (Fig. S13). Considering the promotion of cobalt leaching under acidic conditions, the recycle tests were also performed with pH adjustment back to 7.0, after the PMS addition. In this way, not only the leaching amount is effectively controlled, but also the degradation rate is obviously accelerated. The amount of cobalt leached into solution is merely 0.05 and 0.22 mg/L at the 1st and 5th cycle, respectively (Table S5). Besides, 60% 2-CP still can be degraded in 5 min at the 5th cycle (Fig. 9b). Furthermore, the XRD pattern shows that after reaction, the crystalline structure of catalyst remains unchanged (Fig. S14), and the multi-shelled structure is also well maintained (Fig. S15). It should be mentioned that the thickness of outer and inner shells declines to 60 nm and 120 nm under the acidic condition due to cobalt leaching, respectively (Fig. S15a), while it seems almost unchanged at the neutral pH. The result shows that Co_3O_4 TS-HM-0.7 not only possesses high catalytic activity, but also exhibits good reusability.

4. Conclusions

We proposed an intriguing Co_3O_4 multishelled hollow microreactor to confine PMS activation and 2-CP degradation into multiple void cavities but reject macromolecules HA. To explore the structure-performance relationship of MS-HMs, the shell number, thickness and porosity are tailored by regulating the calcination temperature and reactant molar ratio, respectively. Benefitting from rich active sites, strong capacity of Co^{II} regeneration and good structural integrity, TS-HM exhibit the best catalytic activity as compared to DS-HM and QS-HM. By further tuning the shell thickness and porosity, the catalytic selectivity is regulated due to the size exclusion effect of the shells. For Co_3O_4 TS-HMs-0.7/PMS system, 100% removal of 2-CP was achieved in 3 min with the degradation rate of 1.1334 min^{-1}, at initial pH of 10. Besides, it also demonstrates an excellent universality for halogenated phenols and favorable applicability in actual waters. The underlying mechanism was revealed by XPS, EPR and quenching experiments. It is found that the $O_2^{\cdot-}$ on the catalyst surface plays an important role in accelerating the regeneration of Co^{II} and ·OH and $SO_4^{\cdot-}$ are the dominant ROS for 2-CP degradation. Finally, it should be noticed that, although the main focus of this study is to provide a novel template for the rational design and development of efficient and selective catalysts, future researches are needed to fabricate HoMSs with more eco-friendly compositions.

CRediT authorship contribution statement

Wenqian Li: Conceptualization, Methodology, Formal analysis, Investigation, Data curation, Writing – original draft, Visualization. **Xu He:** Resources, Conceptualization, Writing – view & editing, Supervision, Project administration, Funding acquisition. **Boda Li:** Data curation, Validation, Investigation. **Bin Zhang:** Data curation, Validation. **Ting Liu:** Data curation, Validation. **Ying Hu:** Data curation, Validation, Investigation. **Jun Ma:** Resources, Conceptualization, Writing – review & editing, Supervision, Project administration, Funding acquisition.

Declaration of Competing Interest

The authors report no declarations of interest.

Acknowledgements

This work was supported by the National Key Research and Development Program of China (Grant No. 2019YFD1100104-03-01); National Natural Science Foundation of China (Grant No. 52000048); Cooperative Researching Project of Chunhui Program, Ministry of Education, China (Grant No. HLJ2019006); the Postdoctoral Science Foundation Grant, China (Grant No. 2020T130152); Open Project of State Key Laboratory of Urban Water Resource and Environment, Harbin Institute of Technology (Grant No. QA202008).

Appendix A. Supporting information

Supplementary data associated with this article can be found in the online version at doi:10.1016/j.apcatb.2021.121019.

References

[1] W.J. Tian, H.Y. Zhang, Z. Qian, T.H. Ouyang, H.Q. Sun, J.Y. Qin, M.O. Tadé, S. B. Wang, Bread-making synthesis of hierarchically Co@C nanoarchitecture in heteroatom doped porous carbons for oxidative degradation of emerging contaminants, Appl. Catal. B Environ. 225 (2018) 76–83.

[2] X.Q. Zhou, M.Y. Luo, C.Y. Xie, H.B. Wang, J. Wang, Z.L. Chen, J.W. Xiao, Z. Q. Chen, Tunable S doping from Co_3O_4 to Co_9S_8 for peroxymonosulfate activation: distinguished radical/nonradical species and generation pathways, Appl. Catal. B-Environ. 282 (2021), 119605.

[3] P.J.J. Alvarez, C.K. Chan, M. Elimelech, N.J. Halas, D. Villagrán, Emerging opportunities for nanotechnology to enhance water security, Nat. Nanotechnol. 13 (2018) 634–641.

[4] R. Das, C.D. Vecitis, A. Schulze, B. Cao, A.F. Ismail, X.B. Lu, J.P. Chen, S. Ramakrishna, Recent advances in nanomaterials for water protection and monitoring, Chem. Soc. Rev. 46 (2017) 6946–7020.

[5] J.S. Qian, X. Gao, B.C. Pan, Nanoconfinement-mediated water treatment: from fundamental to application, Environ. Sci. Technol. 54 (2020) 8509–8526.

[6] H. Qiu, M.C. Ye, M.D. Zhang, X.L. Zhang, Y. Zhao, J.H. Yu, Nano-hydroxyapatite encapsulated inside an anion exchanger for efficient defluoridation of neutral and weakly alkaline water, ACS EST Eng. 1 (2020) 46–54.

[7] B.C. Hodges, E.L. Cates, J.H. Kim, Challenges and prospects of advanced oxidation water treatment processes using catalytic nanomaterials, Nat. Nanotechnol. 13 (2018) 642–650.

[8] D. Luo, Y.P. Deng, X.L. Wang, G.R. Li, J. Wu, J. Fu, W. Lei, R.L. Liang, Y.S. Liu, Y. L. Ding, A.P. Yu, Z.W. Chen, Tuning shell numbers of transition metal oxide hollow microspheres toward durable and superior lithium storage, ACS Nano 11 (2017) 11521–11530.

[9] H. Tian, X.Y. Liu, L.B. Dong, X.M. Ren, H. Liu, C.A.H. Price, Y. Li, G.X. Wang, Q. H. Yang, J. Liu, Enhanced hydrogenation performance over hollow structured Co-CoOx@N-C capsules, Adv. Sci. 6 (2019), 1900807.

[10] G. Prieto, H.R. Tüysüz, N. Duyckaerts, J. Knossalla, G.H. Wang, F. Schüth, Hollow nano- and microstructures as catalysts, Chem. Rev. 116 (2016) 14056–14119.

[11] X.R. You, C.Y. Huang, W. Huang, G.Y. Shi, J.J. Deng, T.S. Zhou, Ultra-small CoOx/GO catalyst supported on ITO glass obtained by electrochemical post-treatment of a redox-active infinite coordination polymer: a portable reactor for real-time monitoring of catalytic oxidative degradation of colored wastewater, Environ. Sci. Nano 7 (2020) 554–570.

[12] J.Y. Wang, N.L. Yang, H.J. Tang, Z.H. Dong, Q. Jin, M. Yang, D. Kisailus, H.J. Zhao, Z.Y. Tang, D. Wang, Accurate control of multishelled Co_3O_4 hollow microspheres as high-performance anode materials in lithium-ion batteries, Angew. Chem. Int. Ed. 52 (2013) 6545–6548.

[13] G.Q. Zhang, X.W. Lou, General synthesis of multi-shelled mixed metal oxide hollow spheres with superior lithium storage properties, Angew. Chem. Int. Ed. 53 (2014) 9187–9190.

[14] K.X. Zhu, C.Z. Jin, C.X. Zhao, R.S. Hu, Z. Klencsár, G.A. Sundaram, D.F. Srankó, R. Ge, J.H. Wang, Modulation synthesis of multi-shelled cobalt-iron oxides as efficient catalysts for peroxymonosulfate-mediated organics degradation, Chem. Eng. J. 359 (2019) 1537–1549.

[15] M. Zhang, C.M. Xiao, X. Yan, S.S. Chen, C.H. Wang, R. Luo, J.W. Qi, X.Y. Sun, L. J. Wang, J.S. Li, Efficient removal of organic pollutants by metal–organic framework derived Co/C yolk–shell nanoreactors: Size-exclusion and confinement effect, Environ. Sci. Technol. 54 (2020) 10289–10300.

[16] T. Zeng, X.L. Zhang, S.H. Wang, H.Y. Niu, Y.Q. Cai, Spatial confinement of a Co_3O_4 catalyst in hollow metal–organic frameworks as a nanoreactor for improved degradation of organic pollutants, Environ. Sci. Technol. 49 (2015) 2350–2357.

[17] M.M. Titirici, M. Antonietti, A. Thomas, A generalized synthesis of metal oxide hollow spheres using a hydrothermal approach, Chem. Mater. 18 (2006) 3808–3812.

[18] C. Dong, Q. Yu, R.P. Ye, P.P. Su, J. Liu, G.H. Wang, Hollow carbon sphere nanoreactors loaded with PdCu nanoparticles: Void-confinement effects in liquid-phase hydrogenations, Angew. Chem. Int. Ed. 59 (2020) 18374–18379.

[19] S.J. Gregg, K.S.W. Sing, Adsorption, surface area, and porosity, Academic Press, New York, 1982, p. 303.

[20] T.J. Chuang, C.R. Brundle, D.W. Rice, Interpretation of the x-ray photoemission spectra of cobalt oxides and cobalt oxide surfaces, Surf. Sci. 59 (1976) 413–429.

[21] R.F. Nie, J.J. Shi, W.C. Du, W.S. Ning, Z.Y. Hou, F.S. Xiao, A sandwich N-doped graphene/Co_3O_4 hybrid: an efficient catalyst for selective oxidation of olefins and alcohols, J. Mater. Chem. A 1 (2013) 9037–9045.

[22] J.J. Zhu, K. Kailasam, A. Fischer, A. Thomas, Supported cobalt oxide nanoparticles as catalyst for aerobic oxidation of alcohols in liquid phase, ACS Catal. 1 (2011) 342–347.

[23] W.Y. Chen, B. Han, C. Tian, X.M. Liu, S.J. Liang, H. Deng, Z. Lin, MOFs-derived ultrathin holey Co_3O_4 nanosheets for enhanced visible light CO_2 reduction, Appl. Catal. B Environ. 244 (2019) 996–1003.

[24] Z. Cai, Y.M. Bi, E.Y. Hu, W. Liu, N. Dwarica, Y. Tian, X.L. Li, Y. Kuang, Y.P. Li, X. Q. Yang, H.L. Wang, X.M. Sun, Single-crystalline ultrathin Co_3O_4 nanosheets with massive vacancy defects for enhanced electrocatalysis, Adv. Energy Mater. 8 (2018), 1701694.

[25] Z.H. Xiao, Y.C. Huang, C.L. Dong, C. Xie, Z.J. Liu, S.Q. Du, W. Chen, D.F. Yan, L. Tao, Z.W. Shu, G.H. Zhang, H.G. Duan, Y.Y. Wang, Y.Q. Zou, R. Chen, S.Y. Wang, Operando identification of the dynamic behavior of oxygen vacancy-rich Co_3O_4 for oxygen evolution reaction, J. Am. Chem. Soc. 142 (2020) 12087–12095.

[26] J. Sun, C. Xing, H.Y. Xu, F.Q. Meng, Y. Yoneyama, N. Tsubaki, Filter and buffer-pot confinement effect of hollow sphere catalyst for promoted activity and enhanced selectivity, J. Mater. Chem. A 1 (2013) 5670–5678.

[27] Z.Y. Guo, C.X. Li, M. Gao, X. Han, Y.J. Zhang, W.J. Zhang, W.W. Li, Mn−O covalency governs the intrinsic activity of Co-Mn Spinel oxides for boosted peroxymonosulfate activation, Angew. Chem. Int. Ed. 60 (2021) 274–280.

[28] J. Lee, J.C. Park, J.U. Bang, H. Song, Precise tuning of porosity and surface functionality in Au@SiO_2 nanoreactors for high catalytic efficiency, Chem. Mater. 20 (2008) 5839–5844.

[29] Q.S. Liu, T. Zheng, P. Wang, J.P. Jiang, N. Li, Adsorption isotherm, kinetic and mechanism studies of some substituted phenols on activated carbon fibers, Chem. Eng. J. 157 (2010) 348–356.

[30] Y.M. Zhao, D.W. Lu, C.B. Xu, J.Y. Zhong, M.S. Chen, S. Xu, Y. Cao, Q. Zhao, M. Yang, J. Ma, Synergistic oxidation-filtration process analysis of catalytic $CuFe_2O_4$-Tailored ceramic membrane filtration via peroxymonosulfate activation for humic acid treatment, Water Res. 171 (2020), 115387.

[31] P. Eyer, Effects of superoxide dismutase on the autoxidation of 1, 4-hydroquinone, Chem. Biol. Interact. 80 (1991) 159–176.

[32] C.C. Dong, Z.Q. Wang, Z.C. Ye, J.H. He, Z.X. Zheng, X.Q. Gong, J.L. Zhang, I.M. C. Lo, Superoxide radicals dominated visible light driven peroxymonosulfate activation using molybdenum selenide ($MoSe_2$) for boosting catalytic degradation of pharmaceuticals and personal care products, Appl. Catal. B Environ. 296 (2021), 120223.

[33] C. Liu, L.Y. Liu, X. Tian, Y.P. Wang, R.Y. Li, Y.T. Zhang, Z.L. Song, B.B. Xu, W. Chu, F. Qi, A. Ikhlaq, Coupling metal–organic frameworks and g-C_3N_4 to derive Fe@ N-doped graphene-like carbon for peroxymonosulfate activation: upgrading framework stability and performance, Appl. Catal. B Environ. 255 (2019), 117763.

[34] W.X. Qin, G.D. Fang, Y.J. Wang, D.M. Zhou, Mechanistic understanding of polychlorinated biphenyls degradation by peroxymonosulfate activated with $CuFe_2O_4$ nanoparticles: key role of superoxide radicals, Chem. Eng. J. 348 (2018) 526–534.

[35] G.P. Anipsitakis, D.D. Dionysiou, Radical generation by the interaction of transition metals with common oxidants, Environ. Sci. Technol. 38 (2004) 3705–3712.

[36] X.B. Dong, X.D. Duan, Z.M. Sun, X.W. Zhang, C.Q. Li, S.S. Yang, B.X. Ren, S. L. Zheng, D.D. Dionysiou, Natural illite-based ultrafine cobalt oxide with abundant oxygen-vacancies for highly efficient Fenton-like catalysis, Appl. Catal. B Environ. 261 (2020), 118214.

[37] H.Y. Liu, Z.C. Zhang, M. Ren, J.N. Guan, N. Lu, J. Qu, X. Yuan, Y.N. Zhang, Preparation of the CNTs/AG/ITO electrode with high electro-catalytic activity for 2-chlorophenol degradation and the potential risks from intermediates, J. Hazard. Mater. 359 (2018) 148–156.

[38] L.K. Ewa, G. Sprah, S. Harms, Influence of some groundwater and surface waters constituents on the degradation of 4-chlorophenol by the Fenton reaction, Chemosphere 30 (1995) 9–20.

[39] Z. Liu, H.J. Ding, C. Zhao, T. Wang, P. Wang, D.D. Dionysiou, Electrochemical activation of peroxymonosulfate with ACF cathode: Kinetics, influencing factors, mechanism, and application potential, Water Res. 159 (2019) 111–121.

[40] J. Deng, Y.J. Ge, C.Q. Tan, H.Y. Wang, Q.S. Li, S.Q. Zhou, K.J. Zhang, Degradation of ciprofloxacin using α-MnO_2 activated peroxymonosulfate process: Effect of water constituents, degradation intermediates and toxicity evaluation, Chem. Eng. J. 330 (2017) 1390–1400.

[41] G.X. Huang, C.Y. Wang, C.W. Yang, P.C. Guo, H.Q. Yu, Degradation of bisphenol A by peroxymonosulfate catalytically activated with $Mn_{1.8}Fe_{1.2}O_4$ nanospheres: synergism between Mn and Fe, Environ. Sci. Technol. 51 (2017) 12611–12618.

[42] P.J. Duan, X.N. Liu, B.H. Liu, M. Akra, Y.W. Li, J.W. Pan, Q.Y. Yue, B.Y. Gao, X. Xu, Effect of phosphate on peroxymonosulfate activation: Accelerating generation of sulfate radical and underlying mechanism, Appl. Catal. B Environ. 298 (2021), 120532.

[43] W.Z. Tang, C.P. Huang, The effect of chlorine position of chlorinated phenols on their dechlorination kinetics by Fenton's reagent, Waste Manag. 15 (1995) 615–622.

[44] G. Margarida, A.S. Mestre, M.L. Pinto, I. Gulyurtlu, H. Lopes, A.P. Carvalho, Carbon-based materials prepared from pine gasification residues for acetaminophen adsorption, Chem. Eng. J. 240 (2014) 344–351.